Janus coding acoustic metasurface with reflection symmetry breaking

Yugan Tang,[1,*] Ya Zhang,[1,*] Boyang Xie,[1] Hui Liu,[1] Hua Cheng,[1,†] Jianguo Tian,[1,‡] and Shuqi Chen [1,2,§]

[1]*The Key Laboratory of Weak Light Nonlinear Photonics, Ministry of Education, Smart Sensing Interdisciplinary Science Center, School of Physics and TEDA Institute of Applied Physics, Nankai University, Tianjin 300071, China*
[2]*The Collaborative Innovation Center of Extreme Optics, Shanxi University, Taiyuan, Shanxi 030006, China*

Coding metasurfaces with efficient procedures and simple elements have enabled a large number of novel functions in a digital manner. Designs combining coding and functional integration will undoubtedly enhance the efficiency and space utilization of compact systems. Here, we theoretically propose and numerically and experimentally demonstrate an all-passive reflective Janus coding acoustic metasurface, allowing two-faced direction-dependent coding in a decoupled manner. Exquisitely designed double-layer variable-pitch helical structures with smoothly varying acoustic impedance are used to obtain bianisotropic reflection phase responses, which can also be switched to bi-isotropic responses by changing the boundary conditions. The switchable Janus coding metasurface based on the phase state transitions can be programed to achieve switchable functions on one side without affecting the other side. For instance, the asymmetric and symmetric two-faced focusing and unidirectional switching of functions with coding metasurfaces are numerically and experimentally illustrated. We reveal the inherent essence of the structure-caused asymmetric responses and further pave a flexible way to obtain two-faced, independent wavefront operations and functional switching, which exhibit excellent potential for acoustic applications.

I. INTRODUCTION

The propagation direction is a fundamental characteristic of the wave that provides an additional degree of freedom to manipulate the wavefront in compact acoustic systems. In the past few years, most studies on acoustic metasurfaces have tended to focus on their functions in only a single direction, such as wave focusing [1–4], holograms [5–8], and vortex beams [9–11], and have left the directionality property unconsidered. Inspired by this feature, two-faced wavefront modulation schemes have recently received significant attention and opened a new avenue for controlling light or sound [12–23]. As a representative instance, the asymmetric acoustic wave response was previously proposed and obtained, which can realize one-way performance, including unidirectional invisibility [17,18] and unidirectional focusing [19], by breaking the parity-time symmetry with non-Hermitian modulation; on the basis of the diffraction law with multiple reflections, asymmetric sound transmission [20,21] and asymmetric sound vortices [22,23] can also be achieved. These methods can certainly accomplish asymmetric effects for the forward and backward incidences. Nevertheless, owing to the single functions and inflexible manipulation with constrained conditions, it is difficult to realize freely and fully two-faced acoustic wavefront control.

Recently, originating from materials science and chemistry [24–26], a Janus metasurface with two-faced and independent

modulation for two opposite incidences was proposed and has been implemented in optics [27,28]. To extend it to acoustics, a typical strategy for realizing asymmetric regulations with more flexibility is to break the inherent reciprocity of wave propagation, generally utilizing an external bias such as a kinetic fluid medium [29,30], nonlinear materials [31,32], or space-time modulation [33]. Subsequently, the Janus acoustic metasurface was achieved by employing acoustic circulators to acquire highly nonreciprocal transmission [34], which provides greater efficiency and flexibility for multifunctional integration compared with previous studies on asymmetric wavefront operations [16–23]. Although this nonreciprocal modulation is noninteracting for the forward and backward incidences, it usually suffers from complicated designs, active devices, or bulky configurations, which makes it difficult to apply in compact systems. In addition to the aforementioned traditional metasurfaces, as a digital version, coding and programmable metasurfaces offer a powerful tool to digitally control waves [35–39]. Instead of elements with continuous constituent parameters, coding metasurfaces are characterized by digital and discrete codes, which can simplify the designs and procedures.

Thus, in conjunction with coding methods, a simple, ultra-thin, and passive design with two-faced and independent wave front modulations will provide a unique platform for compact acoustic systems to integrate different functions. Here, we propose an all-passive reflective Janus acoustic metasurface with binary direction-dependent coding, which can be engineered independently and accomplish completely two-faced wavefront manipulation. We theoretically and numerically show that 1-bit Janus coding elements with high reflectivities and desired asymmetric reflection phase responses can

---

*These authors contributed equally to this paper.
†Corresponding author: hcheng@nankai.edu.cn
‡Corresponding author: jjtian@nankai.edu.cn
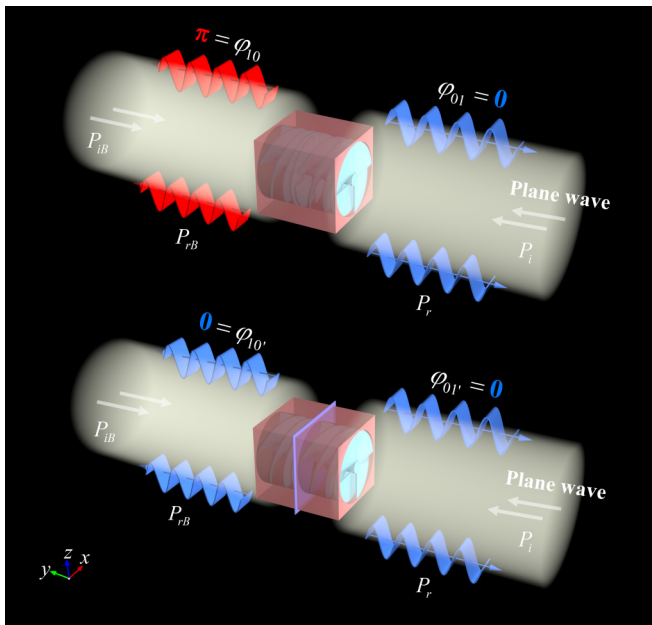§Corresponding author: schen@nankai.edu.cn

FIG. 1. Conceptual illustration of the switchable ACE. A double-layer ACE can produce different reflection phase responses depending on the direction of the incident plane waves. The reflection phase states can be transformed from asymmetric to symmetric by changing the boundary conditions at the center. The blue and red wavefronts indicate the 0 and π phase responses, respectively.

be realized by introducing a helical structure with smoothly varying acoustic impedance and a nonsymmetric boundary to break the reflection symmetry. We uncover the scattering properties of the system and further propose experimental verifications composed of freely asymmetric, symmetric, and switchable functions for opposite incidences at a fixed frequency. The Janus coding approaches may efficiently shift the paradigm in compact acoustic devices and open a different route for all-passive multifunctional acoustic metasurfaces.

II. ASYMMETRIC REFLECTION PHASE RESPONSE WITH SYMMETRY BREAKING

The conceptual schematics of the double-layer asymmetric coding element (ACE) with two phase response states are illustrated in Fig. 1. The asymmetric reflection phase responses of the proposed ACE depend on the direction of the incident waves, as indicated by red and blue arrows at the top of Fig. 1, respectively. The phase response of the ACE can transition from asymmetric to symmetric by changing the boundary condition in the middle, as shown at the bottom of Fig. 1. A single passive reflective coding metasurface programed by the ACE and other coding elements can be designed either to perform different and independent functions on both sides with the asymmetric reflection phase response or to freely switch different functions with the transition of two states. Considering the binary reflective Janus coding metasurfaces, in addition to the conventional 0 and 1 elements with a reflection phase difference of π for incidences in the same direction, it is necessary to design a single element with a phase difference of π for incidences in the forward and backward directions.

To analyze the underlying relations of the reflection phases, we adopt the scattering matrix to describe the input-output relation of a two-port system [18]:

$$S = \begin{pmatrix} t & r_B \\ r & t_B \end{pmatrix}, \qquad (1)$$

where r, r_B, t, and t_B (the subscript B represents the backward incidence) are the corresponding scattering coefficients. The transmission coefficients for opposite incident orientations are the same, $t = t_B$, for a reciprocal system. The energy conservation relation and reciprocity of the acoustic system impose a unitary character on the scattering matrix, which leads to $S^\dagger = S^{-1}$. Thus, a constitutive coupling relation between phases as another form of the unitarity can be concluded [40]:

$$2\varphi_t = \varphi_r + \varphi_{rB} + 2(m+1)\pi, \qquad (2)$$

where m is an integer and φ_t and φ_r (φ_{rB}) are the transmission and reflection phases corresponding to $t = |t|e^{i\varphi_t}$ and $r = |r|e^{i\varphi_r}$ ($r_B = |r_B|e^{i\varphi_{rB}}$), respectively. Although the reflectivities of $R = |r|^2$ and $R_B = |r_B|^2$ on both sides satisfy $R = R_B$ in a lossless system, the reflection coefficients r and r_B can still be different in the reciprocal system, which means that φ_r and φ_{rB} are not necessarily identical and thus provide guidance for the subsequent structural design. According to Eq. (1), the associated eigenvalues can be derived as $\lambda_{1,2} = t \pm \sqrt{rr_B}$, while the eigenvectors can be expressed as $(1, \pm\sqrt{r/r_B})^T$. The eigenvalues and eigenvectors can also be expressed in phase terms as $\lambda_{1,2} = e^{i\varphi_t}(|t| \pm i|r|)$ and $[1, \pm e^{i(\varphi_r - \varphi_{rB})/2}]^T$ by employing Eq. (2). It can be seen that a necessary and sufficient condition to derive conjugated eigenvalues is $\varphi_t = m\pi$. The second components of the eigenvectors are evidently related to the difference between the two reflection phases. An asymmetric reflection phase with a phase difference of π can occur when $e^{i(\varphi_r - \varphi_{rB})/2}$ becomes purely imaginary, which has been achieved at the exceptional point of a broken $\mathcal{PT}$-symmetric system [18,19]. Nevertheless, with high reflectivities on both sides, a simple passive geometric structure with unbroken $\mathcal{PT}$ symmetry can also realize the π phase difference and establish a special coupling relation between eigenvalues and eigenvectors. The details of the asymmetry in the ACE can be found in Sec. B 1.

Classical helical structured acoustic metasurfaces [4,41] with fixed pitch or labyrinthine structures with constant channel height [42] can form two-faced symmetric structures with a constant acoustic impedance. The reflection phases φ_r and φ_{rB} are always equal, that is, $\sqrt{r/r_B} = 1$. We introduce a variable-pitch helical structure with a nonsymmetric boundary to achieve an asymmetric reflection phase response, as shown in Fig. 2(a). The single-layer ACE consists of four individual helical blades spaced at $90°$ to each other connected through a central column, and gradually varying cross sections form between them. The side length of the shell p, blade thickness w, diameter D, inner diameter d, and overall length H can be used to describe its structural properties. The parametric equations for a single helical blade can be written as [43]

$$\begin{aligned} x_r &= R\sin(\omega s), \\ y_r &= R\cos(\omega s), \ s \in [s_1, s_2], \\ z &= C_1(s^n - s_1^n), \end{aligned} \qquad (3)$$
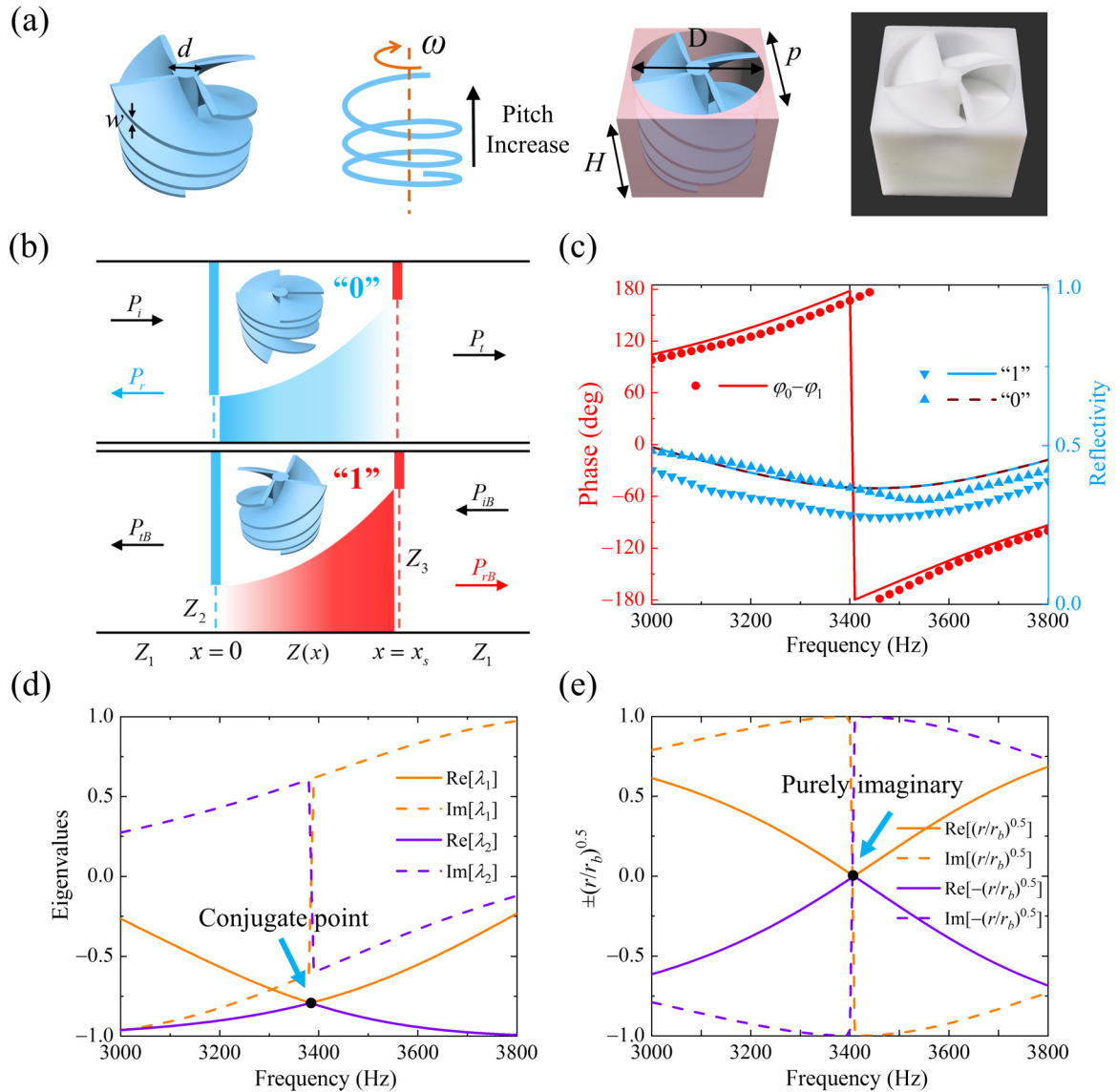
FIG. 2. Design of the single-layer ACE. (a) A variable-pitch helical structure with smoothly varying cross sections consists of four identical blades spiraling around a slender shaft. A photograph of the fabricated single-layer ACE is appended on the right, with $w = 1$ mm, $\omega = \pi/12$, $H = 24.7$ mm, $D = 28$ mm, and $p = 30$ mm. (b) The equivalent cross-sectional view of the single-layer ACE, where the middle layer is assumed to be the route with smoothly varying impedance $Z(x)$. The materials on the left and right are a uniform background medium with impedance Z_1. The top and bottom parts represent the forward and backward propagating cases, respectively. (c) Simulated (lines) and measured (points) reflection spectra and phase difference for the two sides, 0 and 1. The real and imaginary parts of the eigenvalues and the second component of the eigenvectors of the corresponding scattering matrix for the single-layer ACE are shown in (d) and (e), respectively.

where $R = (D + d)/4$ is the rotation radius, s is the rotation time, ω is the angular coefficient, s_1 and s_2 define the range of parameter s, and C_1 is the constant coefficient describing the rate of rise. ωs represents the rotation azimuth angle. The relationship between z and s is nonlinear when $n > 1$. The spiral blade rises following the parametric equations in Eq. (3), resulting in a variable pitch. In terms of the equivalent route, the four identical helical paths of acoustic wave propagation can be combined and totally represented as a hornlike path. The equivalent paths proposed herein are shown in Fig. 2(b), which depicts the cases of forward and reverse incidences. Considering the geometric relations between the helical path and hornlike path, the equivalent coordinate x can be

expressed by its derivative as $dx = \sqrt{(\omega R)^2 + C_1^2 (n s^{n-1})^2}\, ds$. The cross-sectional area of the equivalent path can be derived as $S(x) = 2(D - d)h(x)$, where $h(x) = C_1[(s + \frac{\pi}{2\omega})^n - s^n] - w$ is the height of the single helical path between two adjacent blades. Since $n > 1$, the cross-sectional area gradually varies with x, leading to a gradually varying equivalent acoustic impedance with $Z(x) = \rho c/S(x)$. Using the notation in Fig. 2(b), the acoustic impedances of the throat and mouth are indicated by Z_2 and Z_3, respectively.

To further investigate the presence of the asymmetric reflection phase in the horn path boundaries, the scattering coefficients $r = P_r(0)/P_i(0)$, $r_B = P_{rB}(x_s)/P_{iB}(x_s)$, and $t = P_t(x_s)/P_i(0)$ [using the notation in Fig. 2(b)] can be

analytically derived by utilizing the transfer matrix method (see in Sec. B 1 for details). Thus, by substituting them into Eq. (1), we can readily conclude that

$$\lambda_{1,2} = \frac{2\sqrt{Z_{31}Z_{21}} \pm i\alpha}{(Z_{21} + Z_{31})\cos\varphi(x_s) + (1 + Z_{21}Z_{31})i\sin\varphi(x_s)}, \quad (4)$$

$$\sqrt{r/r_B} = \sqrt{\frac{(Z_{21} - Z_{31})\cos\varphi(x_s) + i(Z_{21}Z_{31} - 1)\sin\varphi(x_s)}{(Z_{31} - Z_{21})\cos\varphi(x_s) + i(Z_{21}Z_{31} - 1)\sin\varphi(x_s)}}, \quad (5)$$

with

$$\alpha = \sqrt{(Z_{21} - Z_{31})^2 \cos^2\varphi(x_s) + (1 - Z_{21}Z_{31})^2 \sin^2\varphi(x_s)},$$

$$\varphi(x) = \int_0^x \sqrt{k^2 - [h'(x)/2h(x)]^2} dx.$$

Here, $Z_1 = \rho c/S_1$ is the acoustic impedance of the incident channel, and $S_1 = \pi D^2/4$. $Z_{21} = Z_2/Z_1$, $Z_{31} = Z_3/Z_1$, and the aforementioned transmission phase is $\varphi_t = \varphi(x_s)$; k, ρ, and c are the wave number, mass density, and speed of sound in air, respectively. The eigenvalues $\lambda_{1,2}$ are conjugate when $\varphi(x_s) = m\pi$ and are independent of $\sqrt{r/r_B}$. When the cross section of the horn path varies smoothly, the asymmetric acoustic impedances of $Z_{21} \neq Z_{31}$ produce an intriguing result. In this case, $\lambda_{1,2}$ and $\sqrt{r/r_B}$ constrain each other, which means the conjugated eigenvalues lead to purely imaginary $\sqrt{r/r_B}$ and vice versa. Moreover, this special coupling relation leads to actual values of 0 and π for φ_r and φ_{rB}, respectively, and not just in a relative sense according to Eq. (2). When $Z_{21} = Z_{31}$, this relation will be broken with full transmission. Thus, by designing the transmission phase $\varphi(x_s)$ of the single-layer ACE as π with asymmetric acoustic impedance, a π phase difference between the reflection phases in opposite directions can be obtained at a given frequency. This treatment proves the capability to separate the two reflection phases on both sides and reveals the relation between the scattering and impedance properties of the equivalent channel. According to Eq. (3), the range of s mainly affects the length of the equivalent path x_s and thus regulates the transmission phase $\varphi(x_s)$. When $\varphi(x_s) = m\pi$, the reflectivity can be expressed as (see Sec. B 1 for details)

$$R = 1 - \frac{4}{2 + Z_{23} + Z_{32}}, \quad (6)$$

which unequivocally shows the relation between reflectivity and the ratios of acoustic impedances on the two boundaries ($Z_{23} = Z_2/Z_3$, $Z_{32} = Z_3/Z_2$). The initial value s_1 and the coefficients C_1 and n mainly control the throat impedance Z_2 with $h(0) = C_1[(s_1 + \frac{\pi}{2\omega})^n - s_1^n] - w$, while C_1 and n also regulate the rate of variation of the impedance and eventually control Z_{23} or Z_{32}. The efficient reflectivities on both sides are also important for reflective Janus regulation, which can be enhanced by increasing Z_{23}. Since $S(x_s)$ has a limitation of S_1, a larger Z_{23} mainly requires a smaller $S(0)$, which can be achieved by regulating s_1, C_1, and n. However, due to the inevitable thermoviscous loss, a smaller $S(0)$ will result in more potential dissipation. To balance reflectivity and loss, the single-layer ACE is intentionally designed with a suitable cross-sectional area to optimize loss through simulation (see Sec. A 1 for details); the double-layer ACE is employed to obtain high re-
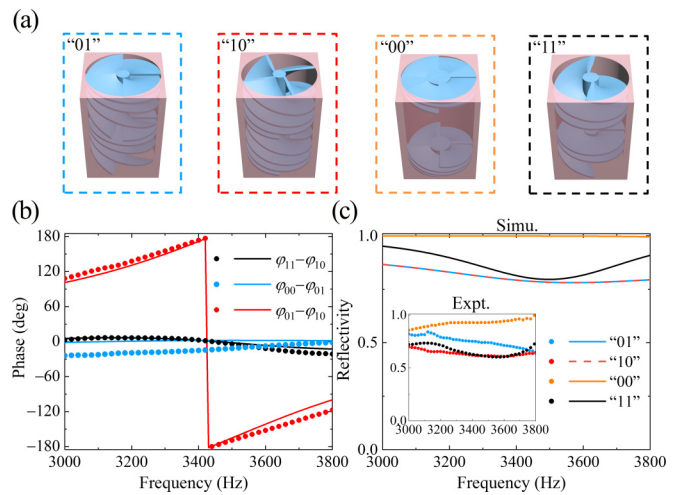

FIG. 3. Design of the Janus coding elements. (a) Schematic of the three Janus coding elements from left to right, which are all composed of a double-layer structure 4.94 cm high. (b) Simulated and experimental phase differences between the three coding elements as binary digital phases. (c) Simulated and experimental reflection spectra. Here, 01 and 10 indicate the normal and reversed states of the double-layer ACE.

flectivity (see Sec. B 2 for details). Based on the well-designed single-layer ACE, we numerically simulated the phase and amplitude of reflected waves on both sides, as illustrated in Fig. 2(c). The phase difference between the two reflections is exactly π around the frequency $f \approx 3400$ Hz. The phases 0 and π (with respect to the incident wave phase) of the Z_2 and Z_3 sides are marked as the digits 0 and 1, respectively. The corresponding experimental results show good agreement with the simulations, except for some slight deviations. The measured phase difference exists with a deviation of 50 Hz from the simulated result, which is approximately 1.5% compared to 3400 Hz. There is also a slight fluctuation in the measured reflectivities, especially the reflectivity of 1, which fluctuates by 0.05 between 3400 and 3800 Hz. These deviations are mainly caused by fabrication errors in three-dimensional (3D) printing and the inevitable gaps between the sample and tube with wave leakage. Optimizing the sealing in the experiment and improving the accuracy of sample preparation can help reduce these deviations. Compared with the simulated reflectivities, the experimental reflection efficiency (defined as the ratio of the experimental value to the simulated value) can reach approximately 80% on the 1 side, while that of the 0 side almost reaches 100%, as shown in Fig. 2(c). Moreover, the simulated results in Figs. 2(d) and 2(e) validate the theoretical predictions, except for some slight frequency deviations. Importantly, the criteria presented herein can be generalizable to lossless media with smoothly varying acoustic impedance rather than confined to a purely geometrical structure.

The double-layer ACE (4.94 cm high) consisting of two layers stacked in sequence is shown in Fig. 3(a), where the digits 01 indicate that the element has a reflection phase response of 0 at the top and π at the bottom and 10 is the reverse of 01. To fabricate a two-faced 1-bit coding metasurface with independent reflected wavefront modulation, the elements 00, with identical reflection phase responses of 0, and 11, with

those of π on both sides, are also designed, as delineated in Fig. 3(a). The three Janus coding elements are similar in size, and all adopt variable-pitch helical structures inside. Essentially, the 01 (or 10) double-layer structure is constructed in a translational manner, and the reflection responses are still asymmetric, while 00 and 11, with C_2-symmetric double-layer structures, possess symmetric reflection responses. Meanwhile, the simulated and experimental reflection phase differences between the three elements are shown in Fig. 3(b), which show good agreement and are 0 or π around a frequency of 3430 Hz. In the theoretical prediction, the π phase difference between the reflection phases for the double-layer ACE requires the same condition as for the single-layer ACE. Since there are some air gaps at the interface between the two layers, the π phase difference for the double-layer ACE has a slight frequency shift compared with the single-layer ACE. In addition, the simulated reflectivities of the three elements can exceed 0.8 for both sides, while the actual reflection efficiencies in the experiment are all over 75%, as depicted in Fig. 3(c). A detailed analysis of the Janus coding elements is given in Sec. B 2. Owing to the difficulty in deriving the equivalent coordinate x analytically, the theoretical results can be used to guide the structural design, and concrete parameter adjustments are realized by simulation.

III. JANUS CODING METASURFACE FOR ASYMMETRIC FOCUSING

The simulated and experimental results of the three Janus coding elements demonstrate that they have the capability to provide accurate two-faced phase differences of 0 and π and high reflectivities to independently regulate the reflected waves for forward and backward directions at a fixed frequency. Based on these direction-dependent coding elements, we first program a one-dimensional Janus Fresnel lens (JFL) with asymmetric reflected focusing to present a function of Janus coding metasurfaces, schematically depicted in Fig. 4(a). The JFL consists of an array of 31 coding elements (total length of 95 cm), generating focal points with different focal lengths for plane wave irradiations in opposite directions. The sequences of the coding elements on both sides of the metasurface can be obtained by utilizing the interference principle, which is supposed to produce constructive interference at the focal point. For the two successive zones i and $i + 1$ on either side of the JFL, the radii r_i and r_{i+1} (from the center of the zone) should satisfy [36]

$$\sqrt{r_{i+1}^2 + f^2} - \sqrt{r_i^2 + f^2} = \frac{\lambda}{2}, \tag{7}$$

where $r_0 = 0$, f is the focal length, and λ is the wavelength. Subsequently, the focal lengths of the designed JFL are $f_1 = 50$ cm and $f_2 = 60$ cm for incidences in the forward and backward directions, respectively. Thus, we can acquire the zone parameters by employing Eq. (7), i.e., $r_1 = 22.9$ cm, $r_2 = 33.2$ cm, and $r_3 = 41.5$ cm for f_1 and $r_1' = 25.0$ cm, $r_2' = 36.0$ cm, and $r_3' = 45.0$ cm for f_2. The corresponding arrangement of the coding elements is shown in Fig. 4(a). The Janus reflected focusing of the incident plane waves at 3430 Hz can be numerically and experimentally achieved by elaborately designing the JFL, as illustrated in Figs. 4(b) and
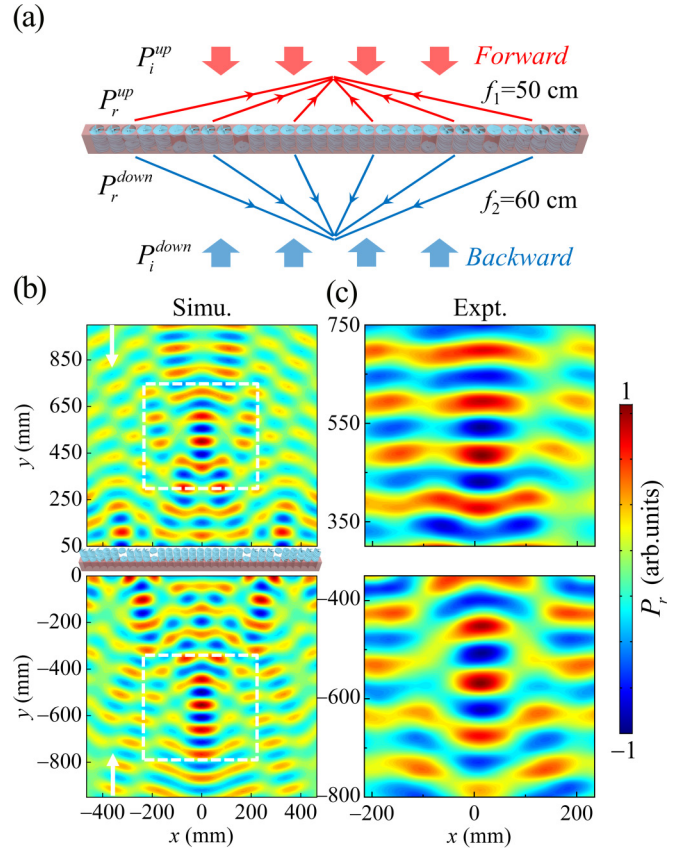

FIG. 4. Janus coding metasurface for asymmetric reflected focusing. (a) Schematic design of a reflective JFL with focal lengths of 50 and 60 cm for normal plane incident waves in the forward and backward directions, respectively. The sequence of the coding elements is consistent with the experiment. (b) Simulated and (c) experimental reflected acoustic pressure distributions at 3430 Hz, where the top and bottom correspond to the forward and backward directions, respectively.

4(c). The reflected sound pressure P_r utilized here is attained by subtracting the pressure without the metasurface from that with the metasurface and normalized by the maximum values. The simulated and experimental focal lengths are 45.0 and 43.5 cm for the incidence in the forward direction, respectively, which are obviously different from those of 55.2 and 57.0 cm for the incidence in the backward direction. The realized JFL exhibits excellent asymmetric focusing properties, and the actual performances are in great agreement with the numerical simulation, which clearly demonstrates the unique characteristic of the variable-pitch helical structure in two-faced reflected wavefront modulations.

IV. SWITCHABLE TWO-FACED WAVEFRONT MANIPULATIONS

To verify the noninteracting reflected wavefront regulations of the metasurface for two opposite incidences and implement a two-faced modulation with high flexibility, we introduce a switchable Janus coding metasurface, which is schematically plotted in Fig. 5(a). The metasurface is composed of only 10 and 01 coding elements and designed
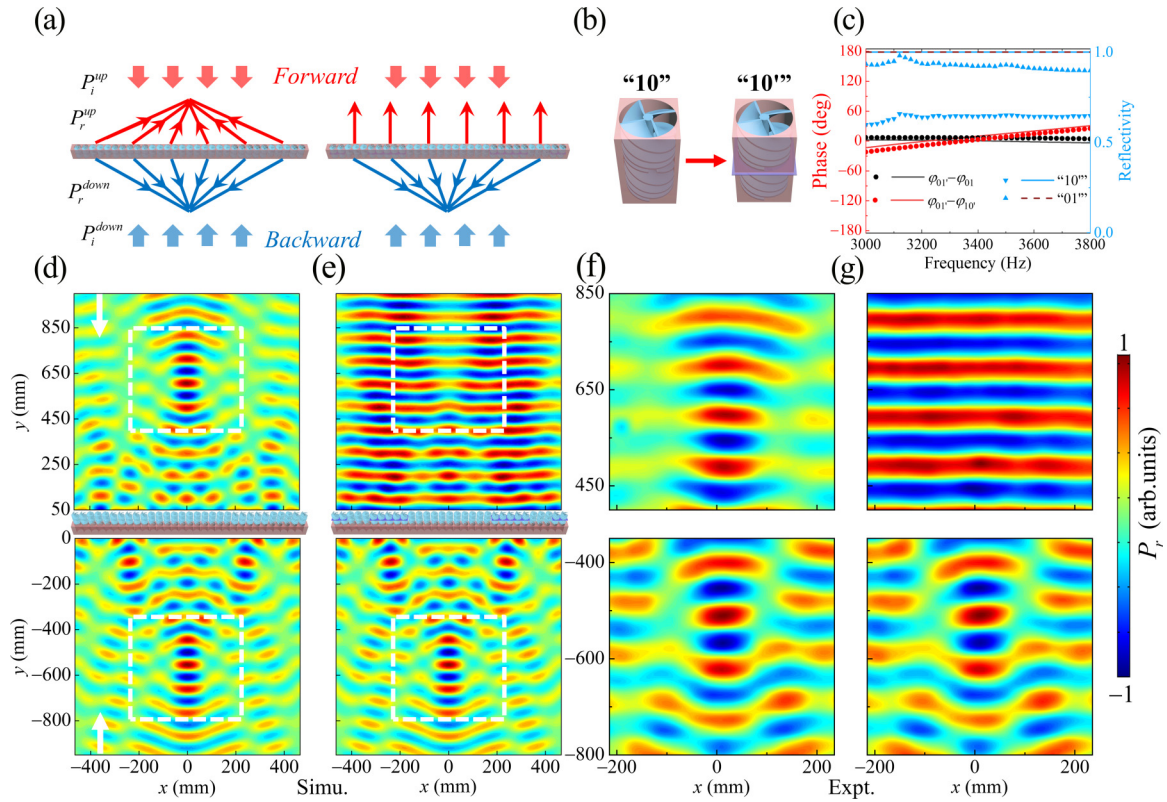
FIG. 5. Switchable Janus coding metasurface. (a) Schematic diagram of the switchable Janus coding metasurface, which can be switched from symmetric reflected focusing for two incident plane waves in opposite directions to the state with unchanged reflected focusing on one side and plane wave irradiation on the other. The schematic switching process of the double-layer ACE is shown in (b), which is achieved by inserting a rigid plate with a thickness of 0.5 mm at the center of the structure. (c) The corresponding reflection spectra and phase differences. (d) The simulated reflected acoustic pressure distributions of the metasurface at 3430 Hz before state switching and (e) the reflected acoustic pressure distributions after state switching. (f) Unswitched and (g) switched corresponding experimental results at 3430 Hz.

with the same focal length of 60 cm for incidences in the forward and backward directions, where the zone parameters have been obtained above and the sequences of elements are shown on the left side of Fig. 5(a). Moreover, the state of the double-layer ACE can be switched from 10 to 10′ (01 indicates the reversal one) by inserting a hard board in the middle of the 10, as shown in Fig. 5(b). Owing to the infinite acoustic impedance in the board boundary, the channel is no longer continuous, and the reflection responses on both sides of 10′ are symmetric at a fixed frequency, i.e., $\sqrt{r/r_B}$ is 1 (with a lossless situation, see in Sec. B 3 for details). Figure 5(c) numerically and experimentally demonstrates that the phase response of the 1 side is switched from π to 0, while that of the 0 side remains 0, where the high reflectivities on both sides can remain at the same time. Similar to the double-layer ACE, the structure with an inserted board is still asymmetric, resulting in different losses. By switching all 10 elements in the metasurface to 10′ and keeping 01 unchanged, as schematically shown on the right side of Fig. 5(a), the reflection phase responses of all elements are 0 for incidence in the forward direction, while those of elements in the backward direction remain the same. Notably, the almost identical phase profile represents the property of a plane wave, where the 0 reflection phase enables the metasurface to be characterized by a hard plane and exhibits great potential for camouflage applications. The simulated reflected acoustic pressure distributions for

both sides of the well-designed metasurface before and after switching at 3430 Hz are displayed in Figs. 5(d) and 5(e), respectively. The corresponding experimental results are shown in Figs. 5(f) and 5(g), respectively, which show excellent focusing characteristics and agree well with the simulations. When we switch the state of the metasurface element from 10 to 10′, the reflected acoustic pressure field for the forward direction can be changed easily from focusing to plane wave radiation, while the reflected focusing for the backward direction is almost impervious. As a consequence, in contrast to the above asymmetric reflected focusing, the presented switchable metasurface not only produces symmetric reflected focusing but also switches to a reflected plane wave on one side without interacting with the function of the other side.

V. CONCLUSIONS

In conclusion, by employing a variable-pitch helical structure to break reflection symmetry, we have introduced a passive switchable direction-dependent ACE and validated numerically and experimentally that it can generate different reflection phase responses or switch to the same responses for two opposite incidences. Based on the ACE and other coding elements, we have proposed and demonstrated the concept of a reflective Janus coding acoustic metasurface, which can be encoded independently in different sequences on both
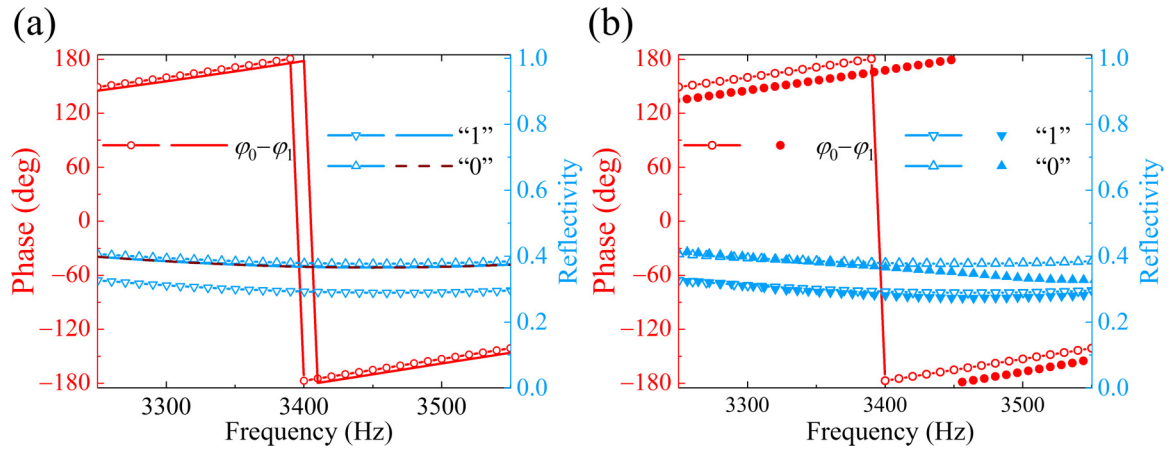
FIG. 6. The thermoviscous loss of the single-layer ACE. (a) Simulated reflection spectra and phase difference for the two sides, 0 and 1, with (lines with data points) and without (lines without points) considering loss. (b) Comparison of experiments (points) and loss simulations (lines with data points) for reflection spectra and phase differences for the two sides, 0 and 1.

sides to achieve noninteracting functions at a fixed frequency. For instance, both asymmetrically focused and symmetrically focused metasurfaces have been constructed using the proposed coding elements, and their performance has been demonstrated numerically and experimentally. Moreover, the switchable metasurface has also been fabricated and illustrated in experiments and simulations. The presented ACE with a simple structure offers a different design methodology for generating an asymmetric reflection response, while the proposed reflective Janus coding metasurface provides a different way of encoding multifunctional metadevices which effectively enhances the space utilization and flexibility of compact systems. Using the switchable ability, the Janus coding metasurface can be developed for unidirectional camouflage and dynamic transformation of imaging in the future.

APPENDIX A: SIMULATION AND EXPERIMENT

1. Simulation

To investigate the wavefront modulation performance of the samples, 3D full-wave simulations are implemented using the commercial COMSOL MULTIPHYSICS software (version 5.6a). The pressure-acoustic module with frequency domain research is employed. The background medium is air with a mass density of $\rho = 1.2$ kg/m^3 and a speed of sound of $c = 343.2$ m/s. The structural walls of the samples are assumed to be rigid boundaries. A cylindrical waveguide with a diameter of 3 cm is used to explore the properties of the coding elements [41]. Additionally, for the simulations of the coding metasurfaces, a rectangular waveguide is utilized with hard boundaries at the top and bottom, perfectly matched layers on

the left and right, and plane wave radiations on the front and back.

To optimize the structure and ensure the reflection efficiency in practical applications, the thermoviscous acoustic module is employed in the metasurface region with two boundary layers $0.2/\sqrt{f/100}$ mm thick, where f is the frequency. The pressure module is used in the incident and transmitted regions. Using the method introduced above, we selected the appropriate parameters s_1, C_1, and n to ensure that $S(0)$ is not too small while $S(x_s)$ remains large, where D and d play an optimization role. The simulated results for the optimized structure with and without considering loss are shown in Fig. 6(a). Compared with the lossless results, the phase differences and reflectivity of 0 are almost the same, while the reflectivity of 1 decreases but still possesses a reflection efficiency of 80%. Although there is a frequency deviation of 60 Hz, approximately 1.8% due to fabrication errors, Fig. 6(b) still shows good agreement between experiment and simulation with loss, which proves the accuracy of our discussion based on thermoviscous loss and provides guidance for designing structures.

2. Experimental measurement

In this section, we introduce the complete experimental procedure. All the samples are manufactured with photosensitive resin via a 3D printer (Lite600, 0.1 mm in precision). Based on the four-microphone method, the reflection spectra of the coding elements are measured in an impedance tube (B&K Transmission Loss Kit Type 4206-T) with 2.9 cm inner diameter tube sections. Four microphones (B&K 4187, 1/4 inch diameter) are inserted into four different positions in the tube. Due to the diameter limitation of the tube, the diameters of the measured elements in cylindrical form are still 2.8 cm, and the total diameters are 2.9 cm, which may be slightly different from the simulations. The experimental setup for the Janus coding metasurface is shown in Fig. 7, which is a waveguide composed of two thick acrylic plates. Sound-absorbing cotton with a thickness of 1.2 cm is placed around the waveguide to mitigate undesired reflections. The size of the entire waveguide is $180 \times 120 \times 3$ cm^3, for which
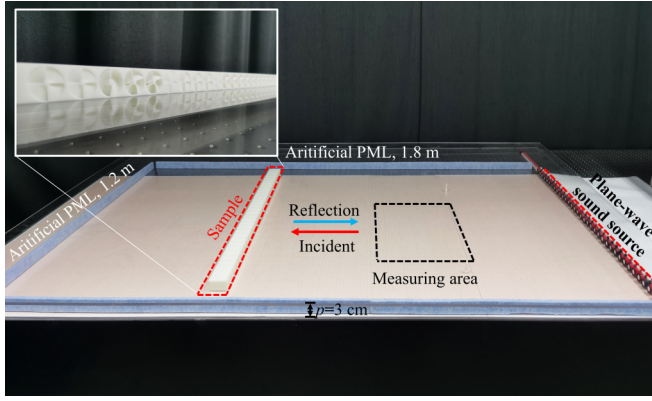
FIG. 7. Photograph of the entire experimental setup for measuring the resultant acoustic field in the specified region on the reflection side of the metasurface. The inset shows the detailed appearance of the metasurface.

the 3 cm spacing equals the side length p of the elements. The sample is firmly sandwiched in the middle of the waveguide. Circular planar speakers with diameters of 2.5 cm are used to form a speaker array at the right boundary as a plane wave source. The measurement area is defined as a rectangular region with dimensions of $45 \times 45 \, \text{cm}^2$, as indicated by the black rectangle in Fig. 7. In the experiment, with a step of 2.5 cm in a frequency range from 3000 to 3800 Hz, the acoustic fields are scanned with one microphone (B&K 4961, 1/4 inch diameter). In addition, a Keysight E5061B ENA vector network analyzer is employed to extract the amplitude and phase of the measured sound signal.

APPENDIX B: METHODS

1. Asymmetry in the asymmetric coding element

To discuss the relation between the structure and the asymmetric reflection responses, the transfer matrix method is employed with the equivalent route of a single-layer ACE in Fig. 2(b). In the present derivation, we assume that the cross section of the systems varies smoothly with negligible lateral velocities and purely real acoustic impedance and that the wavefront varies continuously with the tube section. Acoustic wave propagation in such an equivalent route can be simplified, leading to the one-dimensional wave equation

$$\frac{d^2P(x)}{dx^2} + [\ln S(x)]' \frac{dP(x)}{dx} + k^2 P(x) = 0, \qquad (B1)$$

which is called the Webster equation. When $[\ln S(x)]'$ is not 0, ignoring the second derivative $\varphi(x)''$ (the Wentzel-Kramers-Brillouin approximation), we may readily derive the following:

$$P(x) = \frac{A}{\sqrt{S(x)}} e^{-i\varphi(x)} + \frac{B}{\sqrt{S(x)}} e^{i\varphi(x)}, \qquad (B2)$$

where A and B are constants and the second term appears owing to the finite length of the path. Note that when there is a turning point in the path, that is, $[\ln S(x)]' = 0$, the solution is no longer applicable.

Considering the forward propagating case [see the top part of Fig. 2(b)] of the equivalent model, the propagation relation that involves the output and input conditions can be extracted as

$$\begin{bmatrix} P_i(0) \\ P_r(0) \end{bmatrix} = Q_1 M_0 Q_2 \begin{bmatrix} P_t(x_s) \\ 0 \end{bmatrix}, \qquad (B3)$$

where

$$Q_1 = \frac{1}{2} \begin{bmatrix} 1 + Z_{12} & 1 - Z_{12} \\ 1 - Z_{12} & 1 + Z_{12} \end{bmatrix}$$

and

$$Q_2 = \frac{1}{2} \begin{bmatrix} 1 + Z_{31} & 1 - Z_{31} \\ 1 - Z_{31} & 1 + Z_{31} \end{bmatrix}$$

are the boundary matrices, $Z_{12} = Z_1/Z_2$, and $Z_{31} = Z_3/Z_1$; owing to the anechoic termination at $x \gg x_s$, the reflected sound pressure in the transmission region is 0. In addition, the propagation tensor M_0 completely characterizes the acoustic properties of the equivalent path. Since the sound wave propagates in the equivalent route according to Eq. (B2), the propagation tensor from throat to mouth can be further formulated as

$$M_0 = \sqrt{Z_{23}} \begin{bmatrix} e^{i\varphi(x_s)} & 0 \\ 0 & e^{-i\varphi(x_s)} \end{bmatrix}. \qquad (B4)$$

Therefore, the reflection and transmission coefficients for the forward direction case can be written as

$$t = \frac{2\sqrt{Z_{21}Z_{31}}}{(Z_{21} + Z_{31})\cos\varphi(x_s) + i(Z_{21}Z_{31} + 1)\sin\varphi(x_s)}, \qquad (B5)$$

$$r = \frac{(Z_{21} - Z_{31})\cos\varphi(x_s) + i(Z_{21}Z_{31} - 1)\sin\varphi(x_s)}{(Z_{21} + Z_{31})\cos\varphi(x_s) + i(Z_{21}Z_{31} + 1)\sin\varphi(x_s)}. \qquad (B6)$$

Inverting the orientation of the incident plane wave would change only $Z_{21} - Z_{31} \rightarrow Z_{31} - Z_{21}$, and the reflection coefficient for the backward direction case can be derived as

$$r_B = \frac{(Z_{31} - Z_{21})\cos\varphi(x_s) + i(Z_{21}Z_{31} - 1)\sin\varphi(x_s)}{(Z_{21} + Z_{31})\cos\varphi(x_s) + i(Z_{21}Z_{31} + 1)\sin\varphi(x_s)}. \qquad (B7)$$

On the basis of Eq. (2) and asymmetric acoustic impedance $Z_{21} \neq Z_{31}$, $\varphi_t = \varphi(x_s) = m\pi$ leads to $\varphi_r = 0$ and $\varphi_{rB} = \pi$. Eventually, the reflectivity is derived as

$$R = 1 - \frac{4Z_{21}Z_{31}}{(Z_{21} + Z_{31})^2 \cos^2[\varphi(x_s)] + (1 + Z_{21}Z_{31})^2 \sin^2[\varphi(x_s)]} \qquad (B8)$$

2. Double-layer Janus coding elements

To obtain high reflectivity, double-layer variable-pitch helical structures are utilized. Considering the forward case for 01, where the plane wave is incident on the 0 side, the propagation relation correlating the input pressure to the output pressure is concluded to be

$$\begin{bmatrix} P_i(0) \\ P_r(0) \end{bmatrix} = Q_1 M_0 Q_3 M_0 Q_2 \begin{bmatrix} P_t(2x_s) \\ 0 \end{bmatrix}, \qquad (B9)$$

where

$$Q_3 = \frac{1}{2} \begin{bmatrix} 1 + Z_{32} & 1 - Z_{32} \\ 1 - Z_{32} & 1 + Z_{32} \end{bmatrix}.$$
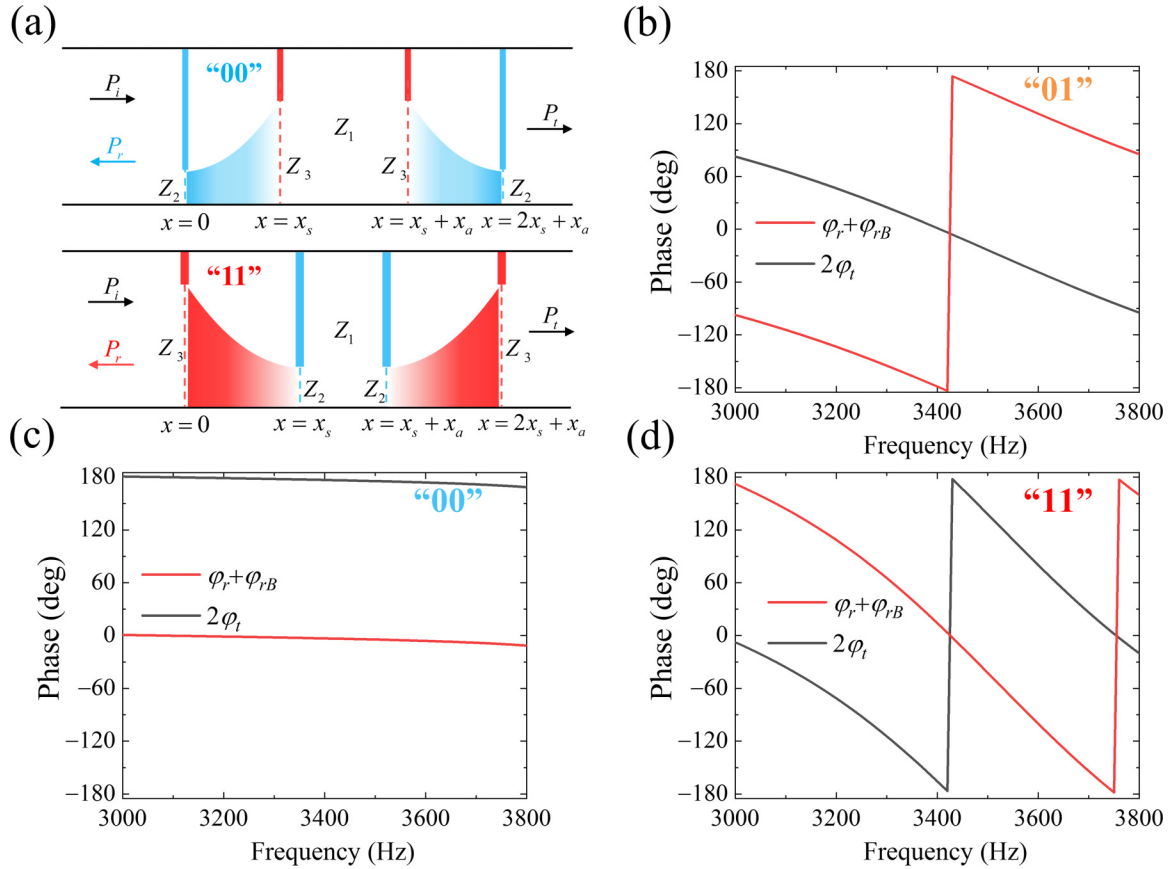
FIG. 8. Equivalent model of the double-layer Janus coding elements and corresponding phase relations. (a) Schematic of the analytical model for 00 and 11. (b)–(d) The intrinsic relations between the transmission and reflection phases for 01, 00, and 11, respectively.

Subsequently, in a similar way, the second components of the eigenvectors for the double-layer ACE can be summarized as

$$\sqrt{r/r_B} = \sqrt{\frac{\cos\varphi(x_s)(Z_{21} - Z_{31}) - i\sin\varphi(x_s)(1 - Z_{21}Z_{31})}{\cos\varphi(x_s)(Z_{31} - Z_{21}) - i\sin\varphi(x_s)(1 - Z_{21}Z_{31})}}.$$
(B10)

For the same condition $\varphi(x_s) = m\pi$, the transmission phase becomes $\varphi_t = 2\varphi(x_s)$, and the eigenvalues are still conjugated. According to Eq. (B10), $\sqrt{r/r_B}$ is also purely imaginary, and $\varphi_r = 0$ and $\varphi_{rB} = \pi$ still exist. The corresponding phase relation is shown in Fig. 8(b). In addition, when $\varphi(x_s) = m\pi$, the reflectivity of the 01 can be expressed as

$$R = 1 - \frac{4}{2 + Z_{23}^2 + Z_{32}^2}.$$
(B11)

In contrast to Eq. (6), the double-layer ACE with the squared term of the impedance ratios certainly increases the reflectivity for the same $Z_{23} > 1$.

The 00 element consists of two channels and an air layer (with a thickness of x_a), as shown in Fig. 8(a). Following the transfer matrix method, the propagation relation of 00 has the form of

$$\begin{bmatrix} P_i(0) \\ P_r(0) \end{bmatrix} = Q_1 M_0 Q_2 M_1 Q_4 M_0' Q_5 \begin{bmatrix} P_t(2x_s + x_0) \\ 0 \end{bmatrix}, \quad \text{(B12)}$$

where

$$Q_4 = \frac{1}{2}\begin{bmatrix} 1 + Z_{13} & 1 - Z_{13} \\ 1 - Z_{13} & 1 + Z_{13} \end{bmatrix},$$

$$Q_5 = \frac{1}{2}\begin{bmatrix} 1 + Z_{21} & 1 - Z_{21} \\ 1 - Z_{21} & 1 + Z_{21} \end{bmatrix},$$

$$M_1 = \begin{bmatrix} e^{i\varphi_a} & 0 \\ 0 & e^{-i\varphi_a} \end{bmatrix}$$

is the propagation tensor for the air layer, $\varphi_a = kx_a$ represents the transmission phase of the air layer, and

$$M_0' = \sqrt{Z_{32}}\begin{bmatrix} e^{i\varphi(x_s)} & 0 \\ 0 & e^{-i\varphi(x_s)} \end{bmatrix}$$

denotes the wave propagation tensor from mouth to throat. Because of the C_2 symmetry and complex form of the reflection coefficient, we consider only one side and set a large mouth with $Z_{31} \approx 1$ and a small throat with $Z_{21} \gg 1$ and $Z_{12} \ll 1$. Therefore, in the limit of $Z_{12}^2 \to 0$, we may simply write

$$r = \frac{1}{1 - 2iZ_{12}\cot[\varphi_a + 2\varphi(x_s)]}, \quad \text{(B13)}$$

which means that the reflection coefficient is always 1 except for the extreme points $\varphi_t = \varphi_a + 2\varphi(x_s) = m\pi$. As long as we avoid the extreme points and use a small throat and a large mouth, the reflection phases φ_r and φ_{rB} of the 00 element will

TABLE I. Design parameters of the double-layer ACE.

Parameter	01 or 10	00	11
d (mm)	5	9	6
s_1	121	121	121
s_2	143.7	139	151.4
C_1	1.2×10^{-22}	1.2×10^{-22}	1.2×10^{-22}
n	10.84	10.7	10.65
ω	$\pi/12$	$\pi/12$	$\pi/12$
Number of blades	4	4	2

always be 0, which causes a constant $2\varphi_t = m\pi$, as shown in Fig. 8(c), and the corresponding reflectivity remains almost 1.

Consequently, by utilizing the same equivalence, the 11 element can also consist of two channels and an air layer, which is displayed in Fig. 8(a). Thus, taking similar conditions with $Z_{31} \approx 1$, $Z_{21} \gg 1$, and $Z_{12} \ll 1$, the reflection coefficient of 11 appears to be

$$r = -\frac{e^{-2i\varphi(x_s)}}{1 - 2iZ_{12} \cot \varphi_a}. \qquad \text{(B14)}$$

When $\varphi(x_s) = m\pi$ and $\varphi_a = (2m+1)\pi/2$, the reflection coefficient is always -1, resulting in the reflection phases $\varphi_r = \varphi_{rB} = \pi$. Because the mouth of 11 is on the outside with more sound waves accessing and reflecting in the inner throat, a small throat causes more loss. To balance loss and reflectivity, the structure of 11 is intentionally designed with a suitable throat to optimize loss; the thickness of the air layer is designed as a quarter wavelength of $x_a \approx 2.5$ cm to obtain high reflectivity. Subsequently, as validated in Fig. 8(d), the reflection phases of 11 are $\varphi_r = \varphi_{rB} = \pi$ around a frequency of 3430 Hz, while the transmission phase becomes $\varphi_t = 2\varphi(x_s) + \varphi_a = (2m+1)\pi/2$. The details of the element design parameters are given in Table I.

3. The state switch caused by the boundary change

Figure 1 schematically exhibits the state switch, which can be achieved by changing the inner boundary of the double-layer ACE. When we insert a hard board in the middle, the acoustic impedance in the board boundary becomes infinite. The sound wave will travel only in a single layer and reflect completely on the hard boundary in the middle. Thus, the wave propagation course can be simplified as a single-layer one, resulting in $Z_{31} \to Z_3/\infty = 0$ for the forward incident plane wave on the 0 side and $Z_{21} \to Z_2/\infty = 0$ for the backward incident plane wave on the 1 side. Following the discussion of the single-layer ACE in Eqs. (B6) and (B7), the reflection coefficient of 01′ can be written as

$$r = \frac{Z_{21} \cos \varphi(x_s) - i \sin \varphi(x_s)}{Z_{21} \cos \varphi(x_s) + i \sin \varphi(x_s)}. \qquad \text{(B15)}$$

Moreover, the reflection coefficient of 10′ is expressed as

$$r_B = \frac{Z_{31} \cos \varphi(x_s) - i \sin \varphi(x_s)}{Z_{31} \cos \varphi(x_s) + i \sin \varphi(x_s)}. \qquad \text{(B16)}$$

When $\varphi(x_s) = m\pi$, both r and r_B become 1, which means symmetric reflection responses on both sides of 01′ (or 10′) around a fixed frequency. Under this condition, the reflection phases of 01′ and 10′ are all 0 and possess the same phase property as the 0 side of 01.

[1] A. Arbabi, Y. Horie, A. J. Ball, M. Bagheri, and A. Faraon, Subwavelength-thick lenses with high numerical apertures and large efficiency based on high-contrast transmitarrays, Nat. Commun. **6**, 7069 (2015).

[2] R. Ghaffarivardavagh, J. Nikolajczyk, R. G. Holt, S. Anderson, and X. Zhang, Horn-like space-coiling metamaterials toward simultaneous phase and amplitude modulation, Nat. Commun. **9**, 1349 (2018).

[3] Y. B. Xie, W. Q. Wang, H. Y. Chen, A. Konneker, B. I. Popa, and S. A. Cummer, Wavefront modulation and subwavelength diffractive acoustics with an acoustic metasurface, Nat. Commun. **5**, 5553 (2014).

[4] S. D. Zhao, A. L. Chen, Y. S. Wang, and C. Z. Zhang, Continuously Tunable Acoustic Metasurface for Transmitted Wavefront Modulation, Phys. Rev. Appl. **10**, 054066 (2018).

[5] G. X. Zheng, H. Muhlenbernd, M. Kenney, G. X. Li, T. Zentgraf, and S. Zhang, Metasurface holograms reaching 80% efficiency, Nat. Nanotechnol. **10**, 308 (2015).

[6] K. Melde, A. G. Mark, T. Qiu, and P. Fischer, Holograms for acoustics, Nature (London) **537**, 518 (2016).

[7] B. Wang, F. L. Dong, Q.-T. Li, D. Yang, C. W. Sun, J. J. Chen, Z. W. Song, L. H. Xu, W. G. Chu, Y.-F. Xiao, Q. H. Gong, and Y. Li, Visible-frequency dielectric metasurfaces for multiwavelength achromatic and highly dispersive holograms, Nano Lett. **16**, 5235 (2016).

[8] Y. F. Zhu, J. Hu, X. D. Fan, J. Yang, B. Liang, X. F. Zhu, and J. C. Cheng, Fine manipulation of sound via lossy metamaterials with independent and arbitrary reflection amplitude and phase, Nat. Commun. **9**, 1632 (2018).

[9] X. Jiang, Y. Li, B. Liang, J. C. Cheng, and L. K. Zhang, Convert Acoustic Resonances to Orbital Angular Momentum, Phys. Rev. Lett. **117**, 034301 (2016).

[10] E. Karimi, S. A. Schulz, I. De Leon, H. Qassim, J. Upham, and R. W. Boyd, Generating optical orbital angular momentum at visible wavelengths using a plasmonic metasurface, Light: Sci. Appl. **3**, e167 (2014).

[11] L. P. Ye, C. Y. Qiu, J. Y. Lu, K. Tang, H. Jia, M. Z. Ke, S. S. Peng, and Z. Y. Liu, Making sound vortices by metasurfaces, AIP Adv. **6**, 085007 (2016).

[12] L. Feng, Y. L. Xu, W. S. Fegadolli, M. H. Lu, J. E. B. Oliveira, V. R. Almeida, Y. F. Chen, and A. Scherer, Experimental demonstration of a unidirectional reflectionless parity-time metamaterial at optical frequencies, Nat. Mater. **12**, 108 (2013).

[13] B. S. Yao, X. F. Zang, Z. Li, L. Chen, J. Y. Xie, Y. M. Zhu, and S. L. Zhuang, Dual-layered metasurfaces for asymmetric focusing, Photonics Res. **8**, 830 (2020).

[14] Y. T. Yang, Y. F. Xu, T. Xu, H. X. Wang, J. H. Jiang, X. Hu, and Z. H. Hang, Visualization of a Unidirectional Electromagnetic Waveguide Using Topological Photonic Crystals Made of Dielectric Materials, Phys. Rev. Lett. **120**, 217401 (2018).

[15] Z. Lin, H. Ramezani, T. Eichelkraut, T. Kottos, H. Cao, and D. N. Christodoulides, Unidirectional Invisibility Induced by $\mathcal{PT}$-Symmetric Periodic Structures, Phys. Rev. Lett. **106**, 213901 (2011).

[16] X. Wang, X. S. Fang, D. X. Mao, Y. Jing, and Y. Li, Extremely Asymmetrical Acoustic Metasurface Mirror at the Exceptional Point, Phys. Rev. Lett. **123**, 214302 (2019).

[17] R. Fleury, D. Sounas, and A. Alu, An invisible acoustic sensor based on parity-time symmetry, Nat. Commun. **6**, 5905 (2015).

[18] X. Zhu, H. Ramezani, C. Shi, J. Zhu, and X. Zhang, $\mathscr{PT}$-Symmetric Acoustics, Phys. Rev. X **4**, 031042 (2014).

[19] T. Liu, X. F. Zhu, F. Chen, S. J. Liang, and J. Zhu, Unidirectional Wave Vector Manipulation in Two-Dimensional Space with an All Passive Acoustic Parity-Time-Symmetric Metamaterials Crystal, Phys. Rev. Lett. **120**, 124502 (2018).

[20] Y. Y. Fu, C. Shen, Y. Y. Cao, L. Gao, H. Y. Chen, C. T. Chan, S. A. Cummer, and Y. D. Xu, Reversal of transmission and reflection based on acoustic metagratings with integer parity design, Nat. Commun. **10**, 2326 (2019).

[21] Y. Li, C. Shen, Y. B. Xie, J. F. Li, W. Q. Wang, S. A. Cummer, and Y. Jing, Tunable Asymmetric Transmission via Lossy Acoustic Metasurfaces, Phys. Rev. Lett. **119**, 035501 (2017).

[22] Y. Y. Fu, Y. Tian, X. Li, S. L. Yang, Y. W. Liu, Y. D. Xu, and M. H. Lu, Asymmetric Generation of Acoustic Vortex Using Dual-Layer Metasurfaces, Phys. Rev. Lett. **128**, 104501 (2022).

[23] Y. Y. Fu, C. Shen, X. H. Zhu, J. F. Li, Y. W. Liu, S. A. Cummer, and Y. D. Xu, Sound vortex diffraction via topological charge in phase gradient metagratings, Sci. Adv. **6**, eaba9876 (2020).

[24] J. Jiang, H. W. Gu, H. L. Shao, E. Devlin, G. C. Papaefthymiou, and J. Y. Ying, Manipulation bifunctional Fe_3O_4-Ag heterodimer nanoparticles for two-photon fluorescence imaging and magnetic manipulation, Adv. Mater. **20**, 4403 (2008).

[25] A. Walther and A. H. E. Muller, Janus particles, Soft Matter **4**, 663 (2008).

[26] Y. B. Zhang, T. T. Tang, C. Girit, Z. Hao, M. C. Martin, A. Zettl, M. F. Crommie, Y. R. Shen, and F. Wang, Direct observation of a widely tunable bandgap in bilayer graphene, Nature (London) **459**, 820 (2009).

[27] K. Chen, G. W. Ding, G. W. Hu, Z. W. Jin, J. M. Zhao, Y. J. Feng, T. Jiang, A. Alu, and C. W. Qiu, Directional Janus Metasurface, Adv. Mater. **32**, 1906352 (2020).

[28] P. Yu, J. X. Li, S. Zhang, Z. W. Jin, G. Schutz, C. W. Qiu, M. Hirscher, and N. Liu, Dynamic janus metasurfaces in the visible spectral region, Nano Lett. **18**, 4584 (2018).

[29] C. P. Wiederhold, D. L. Sounas, and A. Alu, Nonreciprocal acoustic propagation and leaky-wave radiation in a waveguide with flow, J. Acous. Soc. Am. **146**, 802 (2019).

[30] F. Zangeneh-Nejad and R. Fleury, Doppler-based acoustic gyrator, Appl. Sci. **8**, 1083 (2018).

[31] A. M. Mahmoud, A. R. Davoyan, and N. Engheta, All-passive nonreciprocal metastructure, Nat. Commun. **6**, 8359 (2015).

[32] B. I. Popa and S. A. Cummer, Non-reciprocal and highly nonlinear active acoustic metamaterials, Nat. Commun. **5**, 3398 (2014).

[33] J. F. Li, C. Shen, X. H. Zhu, Y. B. Xie, and S. A. Cummer, Nonreciprocal sound propagation in space-time modulated media, Phys. Rev. B **99**, 144311 (2019).

[34] Y. F. Zhu, L. Cao, A. Merkel, S. W. Fan, B. Vincent, and B. Assouar, Janus acoustic metascreen with nonreciprocal and reconfigurable phase modulations, Nat. Commun. **12**, 7089 (2021).

[35] L. L. Li, T. J. Cui, W. Ji, S. Liu, J. Ding, X. Wan, Y. B. Li, M. H. Jiang, C. W. Qiu, and S. Zhang, Electromagnetic reprogrammable coding-metasurface holograms, Nat. Commun. **8**, 197 (2017).

[36] B. Y. Xie, K. Tang, H. Cheng, Z. Y. Liu, S. Q. Chen, and J. G. Tian, Coding acoustic metasurfaces, Adv. Mater. **29**, 1603507 (2017).

[37] B. Y. Xie, H. Cheng, K. Tang, Z. Y. Liu, S. Q. Chen, and J. G. Tian, Multiband Asymmetric Transmission of Airborne Sound by Coded Metasurfaces, Phys. Rev. Appl. **7**, 024010 (2017).

[38] L. Zhang, R. Y. Wu, G. D. Bai, H. T. Wu, Q. Ma, X. Q. Chen, and T. J. Cui, Transmission-reflection-integrated multifunctional coding metasurface for full-space controls of electromagnetic waves, Adv. Funct. Mater. **28**, 1802205 (2018).

[39] Y. Zhang, B. Y. Xie, W. W. Liu, H. Cheng, S. Q. Chen, and J. G. Tian, Anomalous reflection and vortex beam generation by multi-bit coding acoustic metasurfaces, Appl. Phys. Lett. **114**, 091905 (2019).

[40] J. Li, C. Shen, A. Diaz-Rubio, S. A. Tretyakov, and S. A. Cummer, Systematic design and experimental demonstration of bianisotropic metasurfaces for scattering-free manipulation of acoustic wavefronts, Nat. Commun. **9**, 1342 (2018).

[41] X. Zhu, K. Li, P. Zhang, J. Zhu, J. Zhang, C. Tian, and S. Liu, Implementation of dispersion-free slow acoustic wave propagation and phase engineering with helical-structured metamaterials, Nat. Commun. **7**, 11731 (2016).

[42] Y. Li, X. Jiang, R. Q. Li, B. Liang, X. Y. Zou, L. L. Yin, and J. C. Cheng, Experimental Realization of Full Control of Reflected Waves with Subwavelength Acoustic Metasurfaces, Phys. Rev. Appl. **2**, 064002 (2014).

[43] Y. Ding, E. C. Statharas, K. Yao, and M. Hong, A broadband acoustic metamaterial with impedance matching layer of gradient index, Appl. Phys. Lett. **110**, 241903 (2017).